Accepted Article

Title: Oxygen Functional Groups Regulate Cobalt-Porphyrin Molecular Electrocatalyst for Acidic H2O2 Electrosynthesis at Industrial-Level Current

Authors: Yihe Chen, Cheng Zhen, Yubin Chen, Hao Zhao, Yuda Wang, Zhouying Yue, Qiansen Wang, Jun Li, Meng Danny Gu, Qingqing Cheng, and Hui Yang

This manuscript has been accepted after peer review and appears as an Accepted Article online prior to editing, proofing, and formal publication of the final Version of Record (VoR). The VoR will be published online in Early View as soon as possible and may be different to this Accepted Article as a result of editing. Readers should obtain the VoR from the journal website shown below when it is published to ensure accuracy of information. The authors are responsible for the content of this Accepted Article.

RESEARCH ARTICLE

Oxygen Functional Groups Regulate Cobalt-Porphyrin Molecular Electrocatalyst for Acidic H₂O₂ Electrosynthesis at Industrial-Level Current

Yihe Chen,[a,b] Cheng Zhen,[c,d] Yubin Chen,[b] Hao Zhao,[b] Yuda Wang,[b] Zhouying Yue,[b] Qiansen Wang,[a,b] Jun Li,[b] M Danny Gu,[d] Qingqing Cheng,*[b] and Hui Yang*[a,b]

[a]   Y. Chen, Q. Wang, H. Yang
        School of Physical Science and Technology
        ShanghaiTech University
        Shanghai, 201210, P. R. China

[b]   Y. Chen, Y. Chen, H. Zhao, Y. Wang, Z. Yue, Q. Wang, J. Li, Q. Cheng, H. Yang
        Shanghai Advanced Research Institute
        Chinese Academy of Sciences
        Shanghai, 201210, P. R. China
        E-mails: chengqq@sari.ac.cn, yangh@sari.ac.cn

[c]   C. Zhen
        Department of Materials Science and Engineering
        Southern University of Science and Technology
        Shenzhen, Guangdong, 518055, P. R. China

[d]   C. Zhen, M Danny Gu
        Eastern Institute for Advanced Study
        Eastern Institute of Technology
        Ningbo, Zhejiang, 315200, P. R. China

        Supporting information for this article is given via a link at the end of the document.

Abstract: Electrosynthesis of hydrogen peroxide (H_2O_2) based on proton exchange membrane (PEM) reactor represents a promising approach to industrial-level H_2O_2 production, while it is hampered by the lack of high-efficiency electrocatalysts in acidic medium. Herein, we present a strategy for the specific oxygen functional group (OFG) regulation to promote the H_2O_2 selectivity up to 92% in acid on cobalt-porphyrin molecular assembled with reduced graphene oxide. In-situ X-ray adsorption spectroscopy, in-situ Raman spectroscopy and Kelvin probe force microscopy combined with theoretical calculation unravel that different OFGs exert distinctive regulation effects on the electronic structure of Co center through either remote (carboxyl and epoxy) or vicinal (hydroxyl) interaction manners, thus leading to the opposite influences on the promotion in $2e^-$ ORR selectivity. As a consequence, the PEM electrolyzer integrated with the optimized catalyst can continuously and stably produce the high-concentration of ca. 7 wt% pure H_2O_2 aqueous solution at 400 mA cm^{-2} over 200 h with a cell voltage as low as ca. 2.1 V, suggesting the application potential in industrial-scale H_2O_2 electrosynthesis.

Introduction

Anthraquinone oxidation-reduction process is a traditional method for the synthesis of hydrogen peroxide (H_2O_2), but it suffers from the high energy consumption, large organic waste generation and transportation/storage safety issues[1]. Electrochemical oxygen reduction reaction with two-electron pathway ($2e^-$ ORR) has emerged as an attractive alternative to overcome these limitations due to its green attribution and on-site production capability[2]. Although the significant advancement has been achieved in the development of $2e^-$ ORR catalysts in alkaline systems[3], the rapid H_2O_2 decomposition and undesirable membrane stability limit the further development[4]. In contrast, H_2O_2 production in acidic media is well-suited for practical applications owing to good product stability and mature proton exchange membrane (PEM) reactor technology[5], rendering it more desirable to produce H_2O_2 under acidic conditions. Of course, due to the potential presence of special double-layer structure[6] or protonation effects[7] in acidic media, exploring electrocatalysts with excellent performance in acidic conditions is more challenging than that in alkaline conditions. Currently, carbon-based transition metal single atom catalysts (SACs) exhibit the satisfactory $2e^-$ ORR performance due to their isolated active sites, tailored active center and cost-effective[8]. However, the complexity of active centers for typical SACs prepared by pyrolysis at evaluated temperature imposes a significant challenge to gain insight into the structure-activity relationship and underlying catalytic mechanism[9], which will impede the rational design of high-performance catalysts.

RESEARCH ARTICLE

Given that current research is often constrained by unclear regulation mechanisms, molecular catalysts are regarded as a new solution for precise investigation of the electrocatalytic 2e⁻ ORR due to the well-defined atomic structure and adjustable atomic local environment[10]. Noteworthily, for some classical molecular catalysts such as porphyrins and phthalocyanines, although they are commonly served as the excellent model catalysts, the understanding of the regulation mechanism of carrier on active sites is still elusive. In particular, the oxygen-functionalized groups (OFGs) on the carbon supports have been demonstrated to have a great influence on the atomic local microenvironment of the molecular center, thereby tuning the electronic structure and altering the 2e⁻ ORR selectivity[11]. For example, as reported by Sargent et al.[12], OFGs on carbon supports were used to construct an electron-deficient center in the loaded-metalloporphyrin-type molecular catalyst. By altering the quantity of OFGs, the d-band center of the metal was modulated to optimize the adsorption energy of the key intermediate (*OOH), thereby enhancing 2e⁻ ORR performance. Unfortunately, the investigation on the interaction mechanism between OFGs and the active center primarily emphasizes on the effect of "initial" regulation in OFGs on the "final" change in electronic structure of the active site[11b, 12], no work has been devoted to investigating the "process" when the specific OFG interacts with the active center. Such a vague understanding hinders the direct design of the active center, leaving the optimization of *OOH adsorption energy at the level of trial-and-error, thus retarding the development of high-performance molecular catalysts through "OFG strategy". Besides, to get insight into the interaction mechanism between active center and OFGs requires precise control over the specific OFG, but there are few relevant experimental methods.

To this end, we design a series of reduced graphene oxide supported cobalt-porphyrin molecular catalysts (CoTPP@RGO) using a controlled thermal decomposition coupled with π-π stacking strategy. X-ray photoelectron spectroscopy (XPS) proves that the variation of single OFG on the RGO can be precisely controlled at a specific temperature range. X-ray adsorption spectroscopy (XAS), In-situ Raman spectroscopy and Kelvin probe force microscopy (KPFM) reveal that carboxyl and epoxy groups interact with Co centers through the remote interaction while hydroxyl groups directly coordinate with Co center through vicinal interaction, thus resulting in the distinct charge distributions of the Co center. Density functional theory (DFT) verifies that the adsorption energy of key intermediate (*OOH) on the active center regulated by specific OFG is different, unraveling that the remote interaction manner is beneficial to the CoN₄ active site, and hence the optimized 2e⁻ ORR selectivity. The resultant catalyst not only exhibits the H₂O₂ selectivity of 92% on a rotating ring disk electrode (RRDE), but also achieves a steady H₂O₂ production rate of approximately 21 mol h⁻¹ g_cat⁻¹ at a current density of 200 mA cm⁻² in a flow cell, even attaining the unprecedented rate of ~50 mol h⁻¹ g_cat⁻¹ @ 500 mA cm⁻². Significantly, PEM electrolyzer with this catalyst as cathode (fed with pure water at anode) can continuously produce pure H₂O₂ aqueous solution with a high concentration of up to ca. 7 wt% at 400 mA cm⁻² over 200 h with a low cell voltage of ~2.1 V. Our

findings highlight the enormous potential of supported molecular catalysts for the electrosynthesis of H₂O₂ in acidic environment.

Results and Discussion

Synthesis and physical measurements

Figure 1a shows the synthetic approach for preparing the target catalysts (CoTPP@RGO-T, experimental details can be seen in the SI). Firstly, we adjusted the oxygen functionalities on the RGO through a simple thermal treatment under argon atmosphere. Thermal gravimetric (TG, Figure 1b) curve for the GO precursor discloses that the specific OFG can be decomposed at a given temperature range. Based on above phenomena, we can realize the precise control of the content of specific OFG through accurately adjusting the heat-treatment temperature. Accordingly, GO precursor is heating at five specific temperatures (i.e., T=160, 170, 260, 400 and 700 °C) where only single OFG changes to obtain the RGO-T. FT-IR (Figure 1c) confirms the obvious variation in OFGs at a certain temperature range[3a, 13]. To ensure the reliability of the above conclusions, two additional batches of RGO samples were synthesized using the same methods. Both infrared (Figure S1) and XPS (Figure 1d and S2) confirm the good consistency, which guarantees the accurate changes for three types of OFGs in a quantitative manner. Specifically, the variations of C-O-C, -COOH, and -OH occur solely at temperature ranges from 160 to 170, 260 to 400, and 400 to 700 °C, respectively (Figure 1e and S3, detailed calculation process can be seen in the SI). Of note that, the rapid changes in OFGs (Figure S4) are observed in the range of 140-170 °C, verifying the accuracy of OFG variation in such a narrow temperature range (160-170°C). Both FT-IR and XPS verify that the variation in specific OFG could be accurately modulated by controlling the annealed temperature, which provides a premise for us to understand the role of different OFG in regulating the electronic structure of the active center.

The home-made CoTPP molecular, characterized by 1H NMR and UV-Vis (Figure S5 and S6), was self-assembled on the RGO-T carries through π-π stacking (CoTPP@RGO-T). Aberration-corrected scanning transmission electron microscopy (AC-STEM, Figure 1f, 1g and S7) shows the abundant bright dots, corresponding to the atomically dispersed Co atoms, on the graphene matrix, demonstrating the high dispersion of CoTPP molecules without any aggregates on the surface of RGO. The EELS spectrum (Figure 1h) further confirms the presence of Co and N elements[14] on the catalyst, indicative of the successful assembly of CoTPP molecules on RGO-T support. Extended X-ray absorption fine structure (EXAFS) spectra at Co-K edge (Figure 1i) display that no Co-Co scatting paths are detected for the prepared CoTPP@RGO-T catalysts, again attesting the atomic-dispersion of Co atoms on the RGO carrier. Wavelet transform (WT)-XAS (Figure 1j) shows that the WT maximum matches well with that of CoTPP molecular, proving the presence of Co-N bonds. Above results definitely confirm the successful synthesis of supported molecular electrocatalyst with a clear-cut active center.
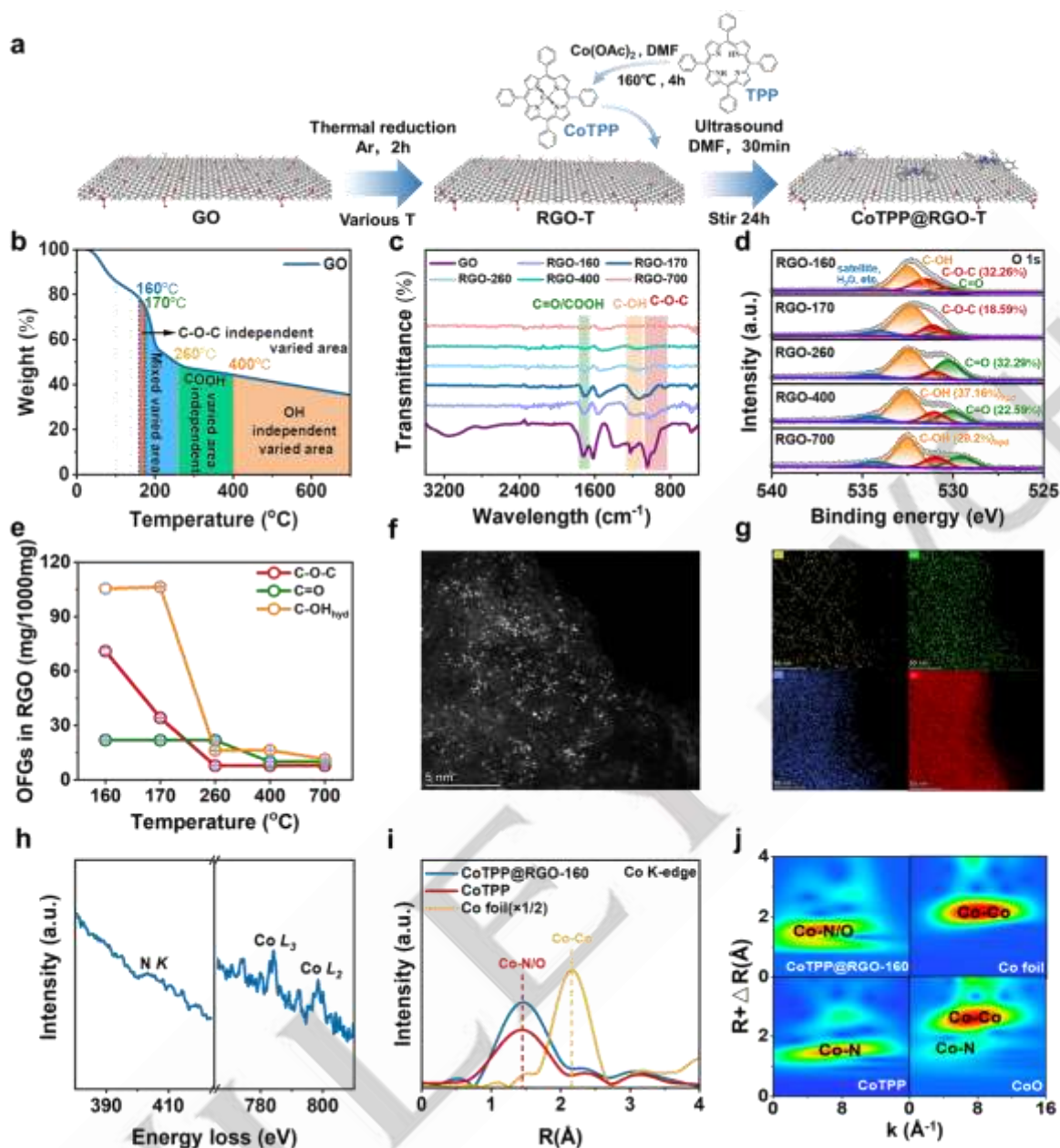
RESEARCH ARTICLE

Figure 1. The synthesis and structural characterizations of CoTPP@RGO catalysts. (a) Schematic diagram for the synthesis of CoTPP@RGO electrocatalyst. (b) TGA curve for the GO under N_2 atmosphere. (c) FT-IR spectra and (d) O 1s high-resolution XPS spectra of RGO carriers annealed at different temperatures. (e) The mass change for the three types of OFGs on the RGO carriers annealed at different temperatures. The error bars correspond to the standard deviation of three independent measurements. (f) AC-STEM image, (g) EDS mapping and (h) EELS spectrum of CoTPP@RGO-160. (i) Co K-edge k^3-weighted FT-EXAFS spectra in R space and (j) WTs for CoTPP@RGO-160 and the reference catalysts (Co foil, CoO and CoTPP).

2e⁻ ORR performance evaluation on RRDE

Liner sweep voltammetry (LSV) on RRDE for various catalysts was conducted to evaluate the catalytic activity and selectivity towards 2e⁻ ORR (Figure 2a and 2b). All the catalysts are tested with an optimal loading of 150 μg cm⁻² (Figure S8). The ORR activities gradually decrease on the CoTPP@RGO-T catalysts as the temperature increasing from 160 to 700 °C, which is probably attributed to the reduced Co sites (Table S2). Above phenomenon also suggests that the OFGs can facilitate the

assembly of CoTPP molecular. As contrast, the pure RGO carrier, CoTPP and TPP molecular (Figure S9 and S10), exhibit much inferior ORR activity than that of CoTPP@RGO-T samples, confirming the combination of CoTPP and RGO carrier can enhance the 2e⁻ ORR performance. As shown in Figure 2b, various samples exhibit the different H_2O_2 selectivity and electron transfer number (N) (the calibrated collection efficiency is ~0.372, Figure S11). Considering the similar electron conductivity and defects (Figure S12 and S13) for CoTPP@RGO-T samples, the differeces in 2e⁻ ORR performance is mainly attributed to the variation of OFGs on the support. With temperature increases

3

RESEARCH ARTICLE

from 160 to 170 °C (corresponding to a decline of C-O-C) and 260 to 400 °C (corresponding to a decline of -COOH), the catalyst displays the obvious decline in H_2O_2 selectivity, with the value from 92 to 70%, 76 to 70% at 0.3 V/RHE, respectively, assessing that the C-O-C and -COOH on RGO carrier play a positive role in promoting the 2e⁻ ORR selectivity. Strikingly, further increase in heat-treatment temperature from 400 to 700 °C (-OH groups decrease) leads to a contineous increase in H_2O_2 selectivity, manifesting that the -OH groups may play a negative effect on the 2e⁻ ORR pathway. Therefore, above electrochemical results corroborate that C-O-C groups on RGO carrier have the greatest positive influence on ORR selectivity, followed by -COOH while -

OH groups favor the 4e⁻ ORR pathway (Figure 2c). Notably, the CoTPP@RGO-T (T=140 and 150 °C) samples show inferior 2e⁻ ORR activity and selectivity compared to the CoTPP@RGO-160, which is possibly due to their poor electron conductivity caused by high oxidation degree (Figure S14)[15]. Simultaneously, the CoTPP@RGO-1000 sample (almost without OFG on support) exhibits the moderate H_2O_2 selectivity among the various CoTPP@RGO-T (160≤T≤700) samples, again proving the effectiveness of OFGs on 2e⁻ ORR performance (Figure S15). Compared to the currently advanced electrocatalysts towards acidic 2e⁻ ORR, our catalyst still belongs to the top tier (Figure 2d).
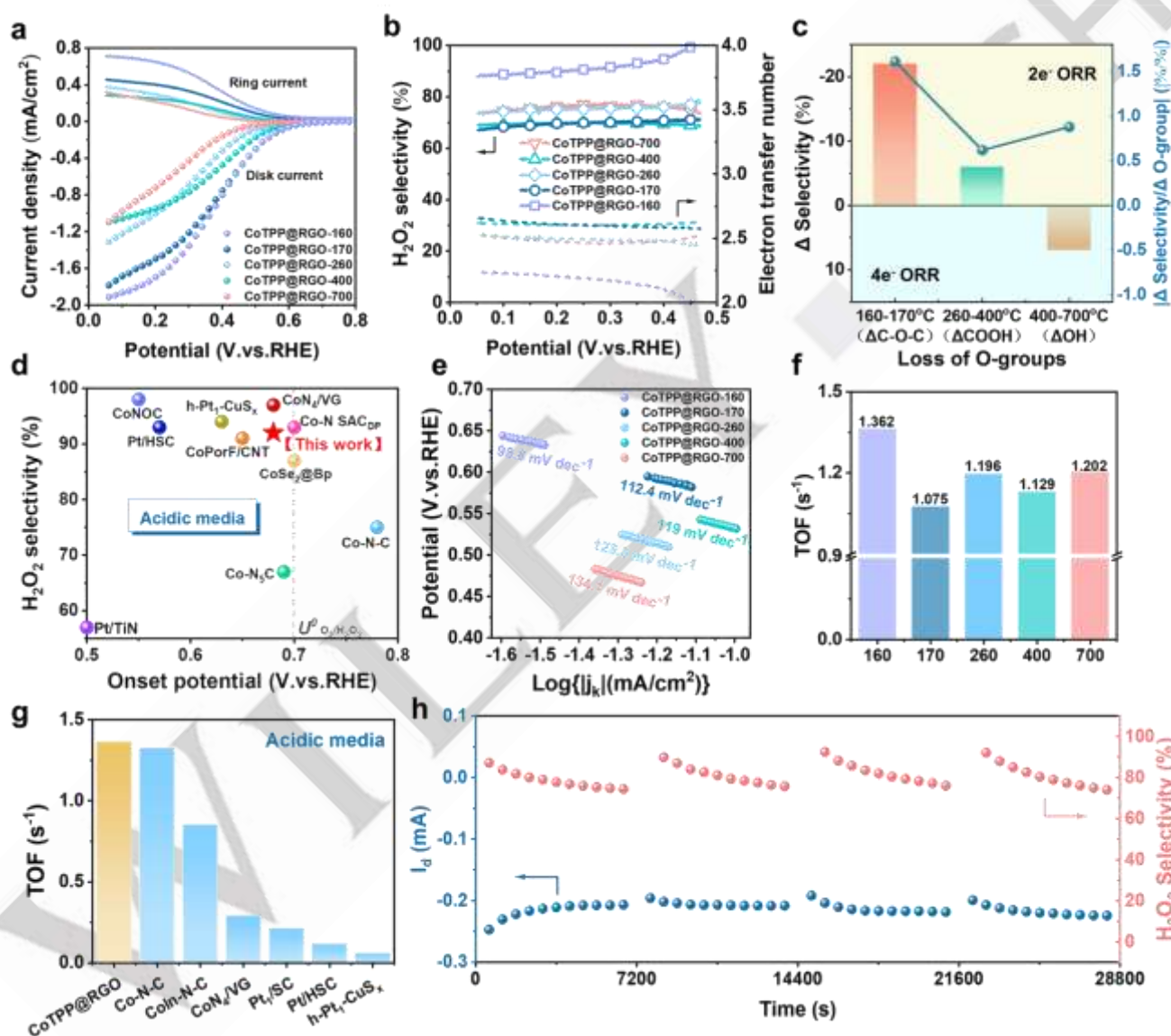

Figure 2. 2e⁻ ORR performance of the CoTPP@RGO-T catalysts on RRDE. (a) LSV curves of 2e⁻ ORR on various CoTPP@RGO-T catalysts in O_2-saturated 0.5 M H_2SO_4 with a rotating rate of 1600 rpm. (b) The calculated H_2O_2 selectivity and electron transfer number as a function of the applied potential. (c) Varying degree of H_2O_2 selectivity induced by the loss degree of different OFGs. (d) The 2e⁻ ORR performance of CoTPP@RGO-160 on RRDE compared with the most advanced acidic catalysts reported recently (Data sources are provided in Table S3). (e) Tafel plots and (f) TOFs @ 0.4 V for various CoTPP@RGO-T catalysts. (g) The comparison for the TOFs of CoTPP@RGO-160 and the most advanced acidic catalysts reported recently (Data sources are provided in Table S4). (h) Stability test for the CoTPP@RGO-160 at a fixed disk potential of ~0.1 V and a fixed ring potential of ~1.4 V.

4

RESEARCH ARTICLE

Tafel plots (Figure 2e) shows that CoTPP@RGO-160 sample exhibits the smallest slope (98.8 mV dec^{-1}), indicative of its fastest kinetics towards 2e$^-$ ORR, which can also be supported by its highest turnover frequency (TOF, Figure 2f). Even when comparing the currently best-performing catalysts, the intrinsic activity of our catalyst places on the best level (Figure 2g). In addition, almost no H_2O_2 reduction current in the presence of 1 mM H_2O_2 at a wide potential window (Figure S16) was observed, ensuring the high H_2O_2 stability. Importantly, the optimized CoTPP@RGO-160 catalyst also exhibits the satisfactory durability with a slight decay of H_2O_2 selectivity after 8 h reaction at a constant potential of 0.1 V (Figure 2h). Above results suggest that the regulation effects of various OFGs on 2e$^-$ ORR performance is distinct, which requires us to further probe into the underlying modulation mechanism.

Interaction mechanism and electronic structure investigation

Prior to explore the modulation effects of specific OFGs on active center, it is crucial to figure out how different OFGs interact with Co center. It is well-known that, as for the catalyst prepared via π-π stacking, the oxygen atoms on the carrier might directly coordinate with Co center or indirectly interact with Co by influencing its local microenvironment, corresponding to the vicinal or remote interaction manners, respectively. Besides, the same OFG may have different interaction manners. First, DFT was performed to calculate the various stable structures and their stabilization energies for different Co-OFGs model structures (Figure 3a and 3b). It can be observed that each OFG forms at least one stable structure, further confirming that all the OFGs can contribute to the assembly of CoTPP molecular. Noteworthily, the direct coordination between -COOH and Co center is unstable, implying that the -COOH may interact with Co center in a remote interaction manner. Meanwhile, the EXAFS spectra of CoTPP@RGO-260 and 400 samples show the similar Co-N/O coordination number (CN) (Figure 3c and Table S5)[16]. Given that only the -COOH groups decrease in this temperature range (i.e., 260-400°C), and the loss of -COOH does not present an influence on the Co-N/O coordination, which further confirms that the -COOH groups should interact with the Co center in a remote interaction manner. Indeed, the self-assembly of CoTPP at room temperature prevents -COOH from direct interaction with the Co center, which is consistent with the literature[3a]. As for C-O-C group, both remote and vicinal interaction manners are existed with the similar stabilization energies. Meanwhile, catalytic volcano plots (Figure 3d) also reveal the similar effects of two C-O-C/Co configurations on 2e$^-$ ORR selectivity. To investigate the actual situation, we conducted EXAFS on the CoTPP@RGO-160 and 170 samples. As shown in Figure 3c and Table S5, the CN of Co-N/O remains the similar for these two samples, suggesting that the decrease of C-O-C groups will not change the local coordination of Co center, clarifying the remote interaction manner between C-O-C and Co center. As for -OH group, there is a significant energy difference between the two configurations (Co-OH-1, Co-OH-2), and the direct coordination mode (OH-2) is energetically more favorable. Besides, two -OH configurations

show the opposite effects on 2e$^-$ ORR selectivity compared to the reference graphene supported CoTPP, and the Co-OH-2 in the vicinal interaction manner lowers the 2e$^-$ ORR selectivity, which matches well with the electrochemical results in Figure 2c. In addition, the CN of Co-N/O shows an obvious decrease (Figure 3c and Table S5) as the temperature increasing from 170 to 260 ℃ (-OH largely decreases), again demonstrating the vicinal interaction manner between -OH and the Co center.

Moreover, KPFM was carried out to further reveal how the -COOH and C-O-C groups regulate the local environment of Co center through the remote interaction manners. Figure 3e shows the KPFM maps of RGO carriers annealed at various temperatures (160, 170, 260 and 400 ℃), and the surface work function (φ) of carbon plane is calculated from the contact potential (Figure 3f, detailed calculation process can be seen in the SI). To be specific, when annealing temperature increases from 160 to 170 ℃ (C-O-C loss) and 260 to 400 ℃ (-COOH loss), the φ shows a significant decrease from 4.799 to 4.517 eV and 4.756 to 4.564 eV, respectively, indicating that the presence of C-O-C and -COOH can increase the work function of RGO, thus leading to a decrease in the electronic delocalization of the RGO surface[17] (Figure 3g and S17). The interlayer charge transfer between CoTPP and RGO will be weakened[18], thus impacting the local environment of the Co center[19]. Above experimental and theoretical investigations illuminate that the Co center interacts with C-O-C or -COOH groups through remote interaction while with -OH by a vicinal interaction manner, which lay a foundation for us to decipher the modulation effects of different OFGs on electronic state of Co center as well as the electrocatalytic 2e$^-$ ORR performance.

In-situ spectroscopic characterizations were performed to accurately examine the interaction manners under operating conditions. In-situ XAS spectroscopy shows that the CNs of Co-N/O under various applied potentials remain consistent with those obtained under ex-situ conditions (Figure 3h, S18 and Table S5), indicating that OFGs maintain their original interaction manners even under working conditions. In-situ electrochemical Raman spectroscopy (Figure 3i) also shows the similar characteristic peaks at different potentials, confirming the excellent stability of the catalyst. Particularly, the characteristic peak at 250 - 300 cm^{-1} does not show stark effect[20] and intensity change at various potentials. Importantly, this Raman shift is also present in the initial state (OCP), signifying that the corresponding species is inherent part of the catalyst. As reported in the literature, such a peak can be attributed to the Co-O bend vibrations of Co-OH[21]. Since no Co-O peaks related to C-O-C and -COOH are observed, the vicinal interaction between -OH and Co center can be also proved under working conditions. Additionally, the *OOH intermediate, a transient species, is captured through time accumulation (Figure 3j). A weak peak appears at 590 - 600 cm^{-1} after electrolysis at 0.1 V vs RHE for 5 minutes, then quickly intensifies to a stable intensity from 5 to 15 min and remains stable until 4 h. Such a Raman shift can be attributed to the Co-O stretching vibrations of Co-OOH[23], demonstrating the formation of *OOH intermediates and a valid 2e$^-$ ORR pathway. Furthermore, the accumulation of *OOH indicates that the rate-
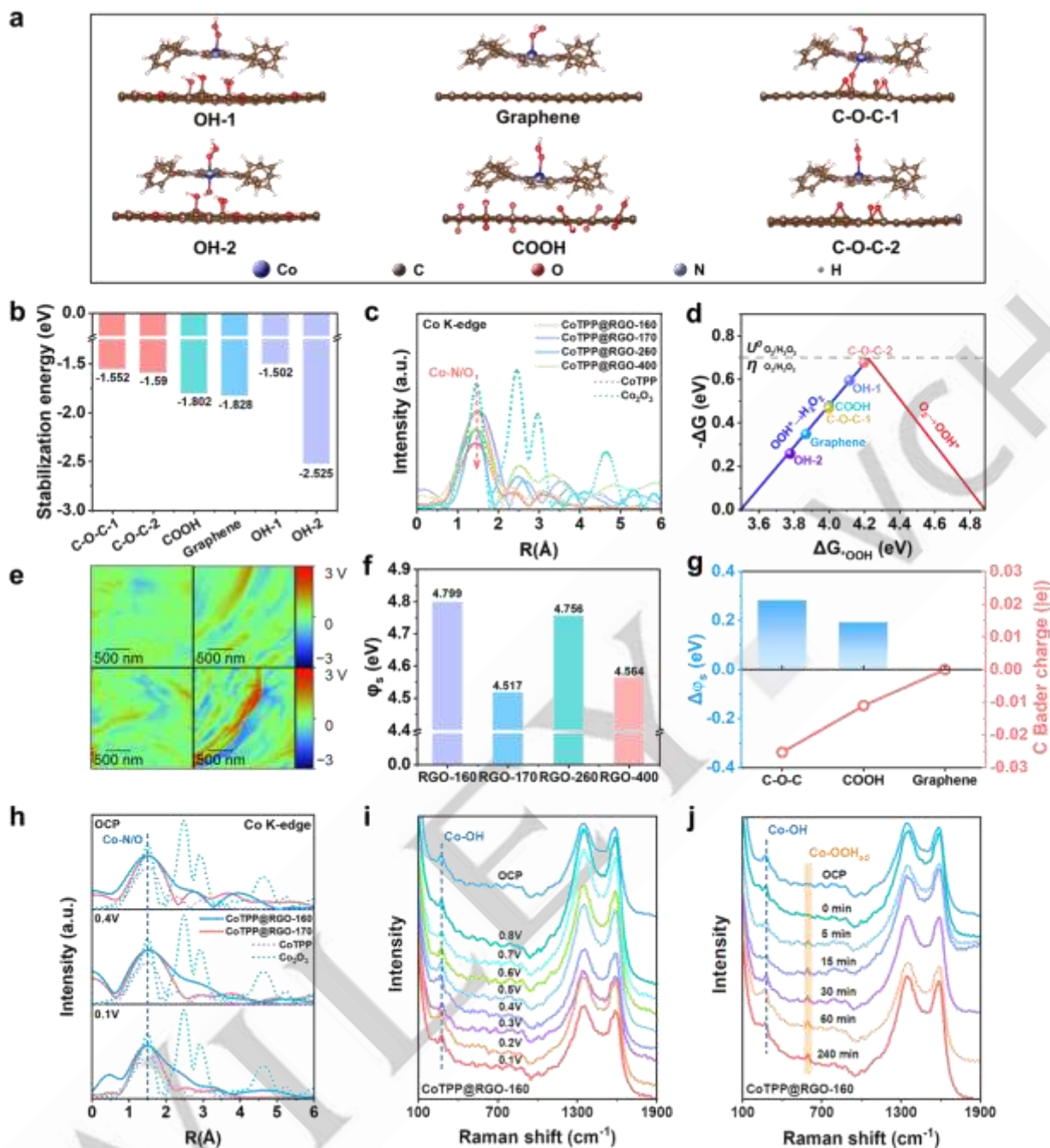
RESEARCH ARTICLE

Figure 3. Interaction mechanism investigation. (a) All stable atomic configurations and (b) corresponding calculated stabilization energies for the Co-OFGs. (c) Calculated Sabatier volcano plot for the 2e⁻ ORR obtained from DFT. The U_L is plotted as a function of ΔG_{*OOH}. The solid lines represent the theoretical Sabatier volcano[22]. (d) Co K-edge k^3-weighted FT-EXAFS spectra in R space for CoTPP@RGO-160, CoTPP@RGO-170, CoTPP@RGO-260, CoTPP@RGO-400 and the reference materials (Co_2O_3 and CoTPP). (e) KPFM maps and (f) surface work functions of RGO-160, RGO-170, RGO-260 and RGO-400. (g) The relationship between the surface work function and Bader charge of different RGO configurations. (h) Co K-edge k^3-weighted FT-EXAFS spectra in R-space obtained from in-situ XAS for CoTPP@RGO-160, CoTPP@RGO-170, and reference materials (Co_2O_3 and CoTPP). (i) In-situ Raman spectra of CoTPP@RGO-160 under various potentials. The laser wavelength is 633 nm. (j) In-situ Raman spectra of CoTPP@RGO-160 at 0.1 V vs RHE.

determining step (RDS) of the reaction is the second step, corresponding to the left leg of volcano (Figure 3d). The stable capture of *OOH over extended time also confirms the robust structure of our catalyst.

As shown in Figure 4b, all the CoTPP@RGO-T samples exhibit higher absorption edge energy than that of the CoTPP,

indicating that the introduction of RGO-T carriers will withdraw the electrons from Co center[24]. Noteworthily, the absorption edge energies of various samples display different variation tendency upon annealing from 160 to 700 °C. Concretely, the adsorption edge of CoTPP@RGO-170 °C or 400 °C shifts to high energy in comparison with that of CoTPP@RGO-160 °C or 260 °C samples,

6

RESEARCH ARTICLE

implying that the existence of C-O-C or -COOH weakens the electron-withdrawing effect. On the contrary, the adsorption edge shifts to low energy when increasing the temperature from 400 to 700 °C when the -OH group is abundantly reduced, disclosing the strong ability of electron-withdrawing for -OH group. Above results suggest that the remote interaction manner (C-O-C and -COOH) is beneficial to alleviate the electron-deficiency around Co center as comparison with the vicinal interaction manner (-OH).

DFT calculations were employed to further study the regulation effects of different OFGs on electron density of Co center as well as the 2e⁻ ORR performance. The Bader charges[25] (Figure 4a and Figure S19) demonstrate that different OFGs on RGO carrier will induce the varying degrees of change in electron density on Co center. Specifically, compared to pure RGO carrier, the introduction of C-O-C and -COOH can enrich the electrons around Co, while -OH prefers to greatly withdraw the electrons from Co sites, which is consistent with the XANES results. The variation in electron density directly leads to varying degrees in d-band shift of Co center (Figure 4c and 4d), consequently altering

the ΔG_{*OOH}[26]. The volcano plots of 2e⁻ ORR performance and ΔG_{*OOH} (Figure S20) displays that all the Co centers modified by OFGs locate at the left leg of volcano-plots (strong absorption side). At this scenario, the larger the ΔG_{*OOH}, the closer to the top of the volcano, and the better the 2e⁻ ORR selectivity. Considering the electron density of Co site is proportional to ΔG_{*OOH} (Figure 4e), the high electron density around Co site is in favor of 2e⁻ ORR. Therefore, the interaction between OFGs and Co center through remote interaction (i.e., C-O-C and -COOH) facilitates 2e⁻ ORR pathway. As expect, the Co-N₄/C-O-C configuration is positioned at the top of the volcano[27], indicative of the superior 2e⁻ ORR performance compared to the other catalysts. The free energy barriers calculated along the 2e⁻ ORR pathway for all models also confirm that the C-O-C group is the most favorable OFG for enhancing the 2e⁻ ORR (Figure 4f and S21). The above discussion reveals the inherent correlation among the types of OFGs, electronic structure of Co and 2e⁻ ORR performance, providing a guidance for the design and synthesis of 2e⁻ ORR catalysts.
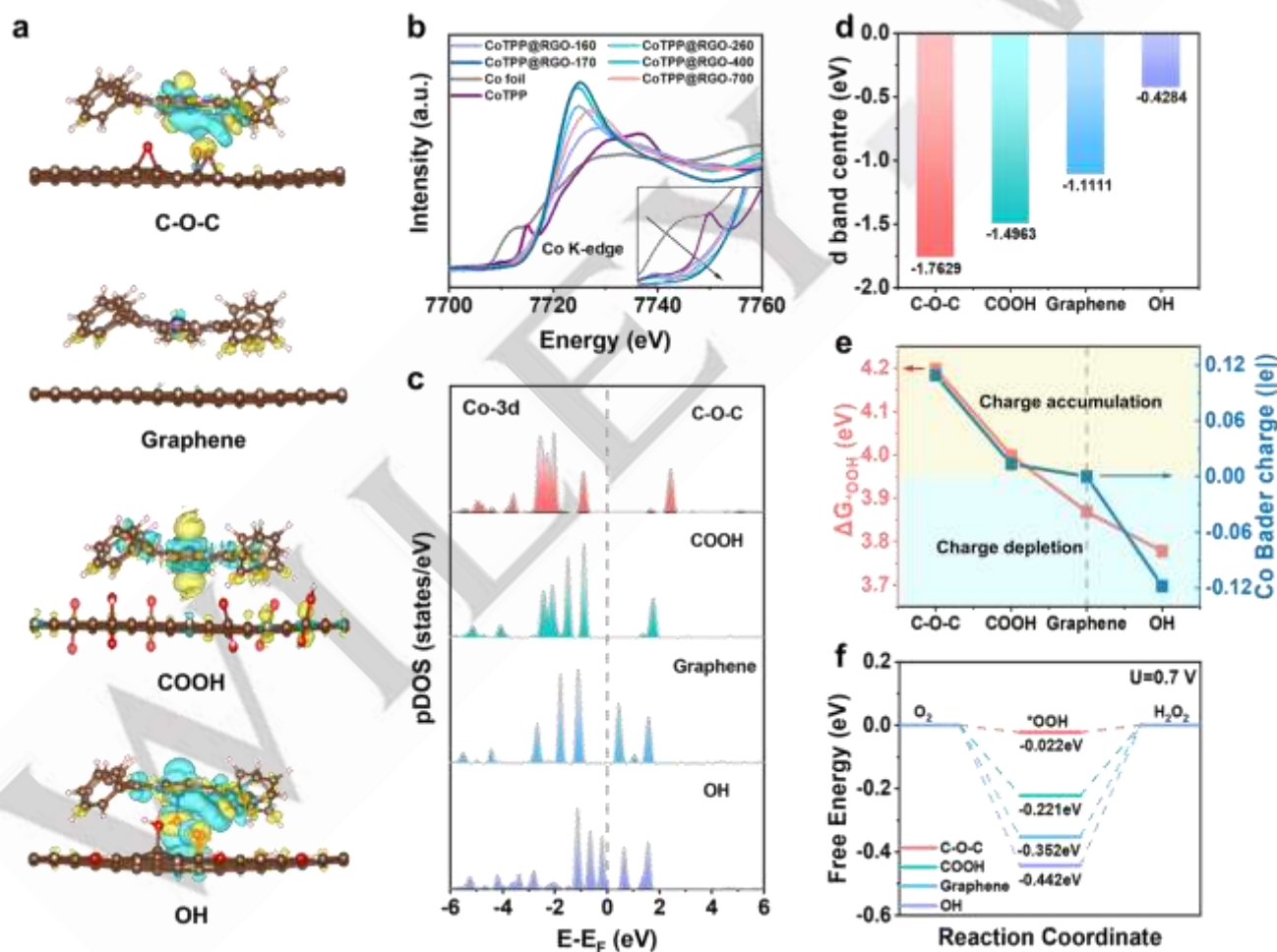

Figure 4. Electronic structure of Co center. (a) Side views of calculated electron density distribution of active centers in various Co-OFGs configurations. Yellow and cyan iso-surfaces represent the electron-accumulation and depletion, respectively. (b) Comparison of the Co K-edge XANES spectra for different CoTPP@RGO-T catalysts. (c) Projected density of states (pDOS) for d-orbitals of Co atoms of Co-N₄/C-O-C, Co-N₄/COOH, Co-N₄/Graphene and Co-N₄/OH configurations. (d) Calculated Co d band center of different Co-OFGs configurations. (e) Calculated *OOH adsorption energies and Bader charge of the Co center in various Co-OFGs configurations. (f) Free-energy diagrams for 2e⁻ ORR pathway at 0.7 V vs RHE.
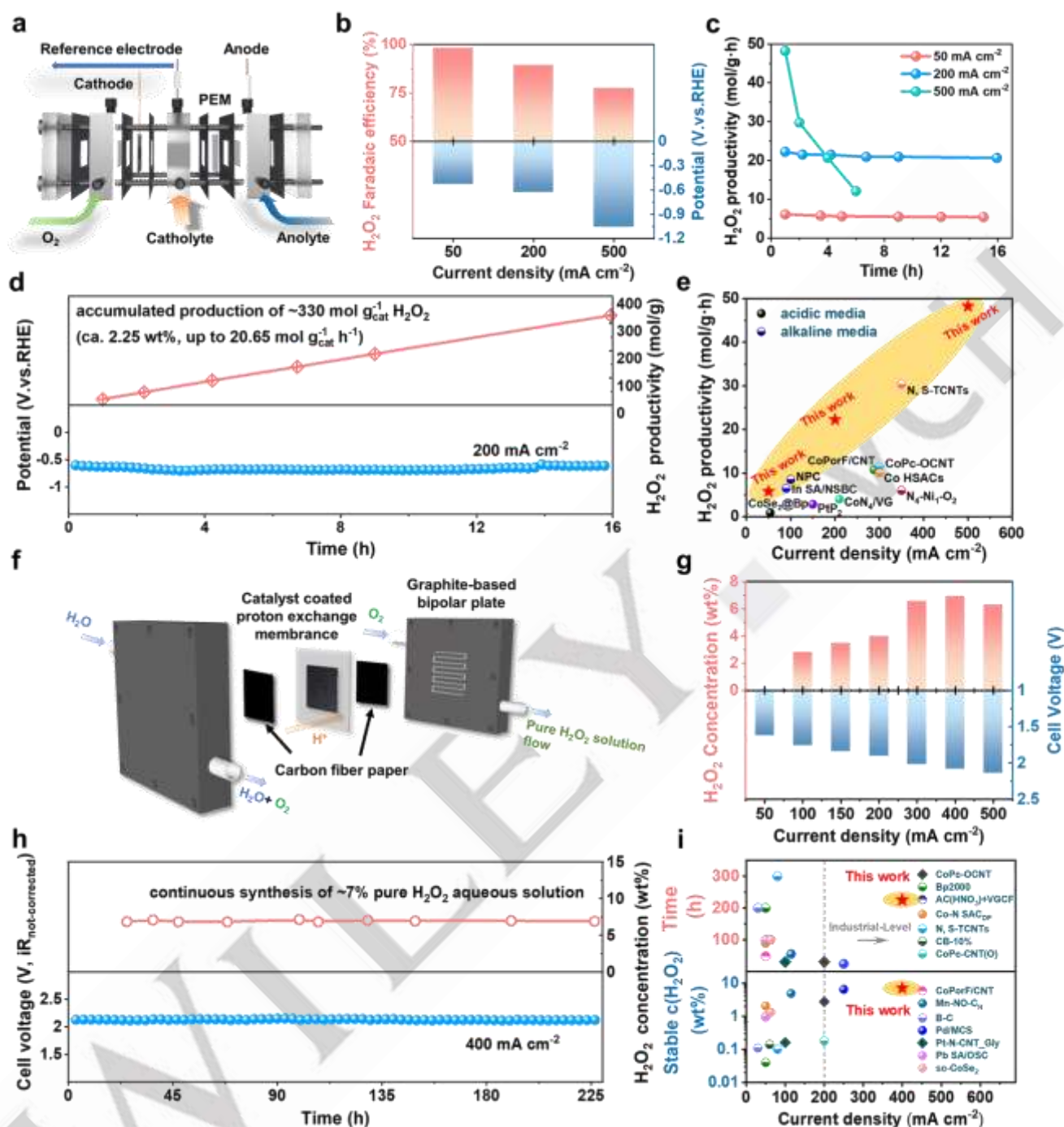
7

RESEARCH ARTICLE

Figure 5. Electrosynthesis of H_2O_2 in flow cell and PEM electrolyzer. (a) Schematic illustration of the flow cell configuration with gas diffusion electrode. (b) FE of H_2O_2 and the corresponding potential profiles. (c) H_2O_2 productivity in a flow cell for 1h at current densities of 50, 200, and 500 mA cm^{-2}, respectively. (d) Stability of CoTPP@RGO cathode for continuous electrosynthesis of H_2O_2 at 200 mA cm^{-2} (75 mL of 0.5 M H_2SO_4 is used as the catholyte, other conditions can be seen in the SI). (e) H_2O_2 production rates of CoTPP@RGOs in the flow cell compared with the most advanced catalysts reported recently (Data sources are provided in Table S6). (f) Schematic diagram of the graphite-based PEM electrolyzer for the continuous production of high-concentration H_2O_2 liquid flow. (g) H_2O_2 concentration and the corresponding potential profiles. (h) Stability of MEA integrated with CoTPP@RGO as cathode for continuous electrosynthesis of pure H_2O_2 liquid flow at current density of 400 mA cm^{-2} in PEM electrolyzer (details can be seen in the SI). (i) A comparison of stable H_2O_2 concentration and stability reported in this case with the most advanced electrocatalysts newly reported under various electrolysis configurations (Data sources are provided in Table S7). For flow cells (except for one-pass flow cell), cumulative concentration is used due to the lack of the data of stable concentration.

8

RESEARCH ARTICLE

Electrosynthesis of H₂O₂ in flow cell and membrane electrode assembly

Flow cell (Figure 5a) was used to evaluate the performance and stability for the electrosynthesis of H_2O_2 at high current density. The galvanostatic electrolysis at 50, 200, and 500 mA cm⁻² was performed (Figure S22). As shown in Figure 5b, the faradaic efficiency (FE) of H_2O_2 is quantified by titration method (experimental details are seen in the SI, Figure S23). Obviously, as the current density increases, the FE gradually decreases, which is attributed to the hydrogen evolution at extremely low potentials (Figure S24). Of note that the FEs calculated from flow cell match well with those on RRDE (Figure S25). Noteworthily, a maximum productivity (Figure 5c) is achieved at a current density of 500 mA cm⁻² with the value of 49 mol h⁻¹ g_{cat}^{-1}. However, a rapid performance decay is simultaneously observed when the current density increases to 500 mA cm⁻², while there is no significant decline in productivity at 50 and 200 mA cm⁻². To explore the underlying reasons, in-situ Raman spectroscopy was employed to analyze the possible structural evolution during the electrolysis. As shown in Figure S26, when the potential decreases to below -0.7 V vs RHE, a new Raman band appears around 540 cm⁻¹. This band can be attributed to the stretching vibration of Co-O in the CoO_x[28], implying that single Co atoms might be detached from molecular skeleton and aggregated into clusters, thus probably interpreting the rapid decay at 500 mA cm⁻². The observed large aggregates in AC-STEM also confirm above speculation (Figure S27). The galvanostatic electrolysis at 200 mA cm⁻² was conducted for 16 hours (Figure 5d) with the stable productivity of H_2O_2 (ca. 21 mol h⁻¹ g_{cat}^{-1}), outperforming the best catalyst reported in the literature (Figure 5e and Table S6). After electrolysis, approximately 2.25 wt% H_2O_2 solution can be obtained.

To avoid post-treatment processes to purify the H_2O_2 solution, PEM electrolyzer (Figure 5f) was assembled to produce pure H_2O_2 aqueous solution. The membrane electrode assembly (MEA) was fabricated by catalyst coating membrane (CCM) method (experimental details can be seen in the SI). The performance was evaluated under the galvanostatic electrolysis mode (Figure S28 and S29). The recorded H_2O_2 concentration and the cell voltage are depicted in Figure 5g. When the current density is above 100 mA cm⁻², the liquid products can be continuously collected from the outlet. In particular, the H_2O_2 concentration is roughly proportional to the current density, reaching the maximum concentration at 400 mA cm⁻². However, a drop in concentration is observed when the current density increases to 500 mA cm⁻² (Figure S30). Subsequently, galvanostatic electrolysis was performed at 400 mA cm⁻² to assess the stability of the catalyst (Figure 5h). Such a PEM electrolyzer can produce pure H_2O_2 aqueous solution stably and continuously with a constant concentration of ca. 7 wt%. Encouragingly, the electrolyzer achieves the groundbreakingly exceptional stability (225 h) at an unprecedentedly low cell voltage (~2.1 V) and the highest industrial-level current density (400 mA cm⁻²) compared to the most advanced electrocatalysts or other novel electrolyzers (Figure 5i and Table S7). It is noting that such high concentration H_2O_2 produced in this case can be continuously collected as liquid

flow, eliminating H_2O_2 accumulation and retrieving midway in batch reactor (Figure S31), which would offer the application potential for large-scale synthesis of high-purity H_2O_2. In addition, XPS spectra of the cathode catalysts after the electrolysis (Figure S32) show that no obvious changes in the O-content and OFGs species were observed on the catalysts, indicative of the good structural-stability for the prepared electrocatalyst even operating under harsh electrolysis conditions. The high dispersion of Co without any aggregates in AC-STEM images further supports this conclusion (Figure S33).

Conclusion

In this work, the variation of the single OFG on the RGO carrier can be accurately tailored at the specific temperature range, and a series of CoTPP@RGO-T catalysts were prepared though self-assembly method. Advanced spectroscopic measurements combined with theoretical calculation have infinitely demonstrated that different OFGs represent the distinguishing interactions on Co center through either remote or vicinal interaction manner, thus inducing the different degrees of electron deficiency around Co center. Given that the correlation between OFGs and 2e⁻ ORR selectivity, the advantageous status of CoN_4 sites has been clarified when influenced by OFGs in remote interaction manner, and the optimal OFG is determined to C-O-C group. As a result, the CoTPP@RGO-160 catalyst with a high proportion of C-O-C groups achieves a 2e⁻ ORR selectivity of 92% on RRDE. PEM electrolyzer integrated with such a catalyst achieves continuous production of pure H_2O_2 aqueous solution with high concentration up to ca. 7 wt% and low cell voltage of ~2.1 V under 400 mA cm⁻² over 200 h, suggesting the application potential in H_2O_2 synthesis.

Acknowledgements

Conflicts of interest

The authors declare no competing financial interest.

[1]   a) R. Gao, L. Pan, Z. Li, C. Shi, Y. Yao, X. Zhang, J. J. Zou, *Adv. Funct. Mater.* **2020**, *30*, 1910539; b) B. Q. Li, C. X. Zhao, J. N. Liu, Q. Zhang, *Adv. Mater.* **2019**, *31*, 1808173.

[2]   Y. Bu, Y. Wang, G. F. Han, Y. Zhao, X. Ge, F. Li, Z. Zhang, Q. Zhong, J. B. Baek, *Adv. Mater.* **2021**, *33*, 2103266.

[3] a) Z. Lu, G. Chen, S. Siahrostami, Z. Chen, K. Liu, J. Xie, L. Liao, T. Wu, D. Lin, Y. Liu, T. F. Jaramillo, J. K. Nørskov, Y. Cui, *Nat. Catal.* **2018**, *1*, 156-162; b) Y. Wang, G. I. N. Waterhouse, L. Shang, T. Zhang, *Adv. Energy Mater.* **2020**, *11*, 2003323; c) Y. Long, J. Lin, F. Ye, W. Liu, D. Wang, Q. Cheng, R. Paul, D. Cheng, B. Mao, R. Yan, L. Zhao, D. Liu, F. Liu, C. Hu, *Adv. Mater.* **2023**, *35*, 2303905; d) M. Wang, N. Zhang, Y. Feng, Z. Hu, Q. Shao, X. Huang, *Angew. Chem. Int. Ed.* **2020**, *59*, 14373-14377; e) S. Chen, T. Luo, K. Chen, Y. Lin, J. Fu, K. Liu, C. Cai, Q. Wang, H. Li, X. Li, J. Hu, H. Li, M. Zhu, M. Liu, *Angew. Chem. Int. Ed.* **2021**, *60*, 16607-16614; f) Q. Yang, W. Xu, S. Gong, G. Zheng, Z. Tian, Y. Wen, L. Peng, L. Zhang, Z. Lu, L. Chen, *Nat. Commun.* **2020**, *11*, 5478.

[4] a) J. M. Campos-Martin, G. Blanco-Brieva, J. L. G. Fierro, *Angew. Chem. Int. Ed.* **2006**, *45*, 6962-6984; b) K. E. Ayers, L. T. Dalton, E. B. Anderson, *ECS Trans.* **2012**, *41*, 27-38.

[5] Y. R. Zheng, S. Hu, X. L. Zhang, H. Ju, Z. Wang, P. J. Tan, R. Wu, F. Y. Gao, T. Zhuang, X. Zheng, J. Zhu, M. R. Gao, S. H. Yu, *Adv. Mater.* **2022**, *34*, e2205414.

[6] P. Li, Y. Jiao, Y. Ruan, H. Fei, Y. Men, C. Guo, Y. Wu, S. Chen, *Nat. Commun.* **2023**, *14*, 6936.

[7] a) J. Herranz, F. Jaouen, M. Lefèvre, U. Kramm, E. Proietti, J. Dodelet, P. Bogdanoff, S. Fiechter, I. Abs-Wurmbach, P. Bertrand, T. Arruda, S. Mukerjee, *J Phys Chem C Nanomater Interfaces.* **2011**, *115*, 24179561; b) M. Rauf, Y.-D. Zhao, Y.-C. Wang, Y.-P. Zheng, C. Chen, X.-D. Yang, Z.-Y. Zhou, S.-G. Sun, *Electrochem. Commun.* **2016**, *73*, 71-74.

[8] a) J. Gao, B. Liu, *ACS Mater. Lett.* **2020**, *2*, 1008-1024; b) X. Guo, S. Lin, J. Gu, S. Zhang, Z. Chen, S. Huang, *ACS Catal.* **2019**, *9*, 11042-11054; c) C. Tang, L. Chen, H. Li, L. Li, Y. Jiao, Y. Zheng, H. Xu, K. Davey, S.-Z. Qiao, *J. Am. Chem. Soc.* **2021**, *143*, 7819-7827.

[9] a) E. Jung, H. Shin, B. H. Lee, V. Efremov, S. Lee, H. S. Lee, J. Kim, W. Hooch Antink, S. Park, K. S. Lee, S. P. Cho, J. S. Yoo, Y. E. Sung, T. Hyeon, *Nat. Mater.* **2020**, *19*, 436-442; b) C. Tang, Y. Jiao, B. Shi, J. N. Liu, Z. Xie, X. Chen, Q. Zhang, S. Z. Qiao, *Angew. Chem. Int. Ed.* **2020**, *59*, 9171-9176.

[10] a) W. Fan, Z. Duan, W. Liu, R. Mehmood, J. Qu, Y. Cao, X. Guo, J. Zhong, F. Zhang, *Nat. Commun.* **2023**, *14*, 1426; b) C. Liu, Z. Yu, F. She, J. Chen, F. Liu, J. Qu, J. M. Cairney, C. Wu, K. Liu, W. Yang, H. Zheng, Y. Chen, H. Li, L. Wei, *Energy Environ. Sci.* **2023**, *16*, 446-459; c) A. W. Nichols, E. N. Cook, Y. J. Gan, P. R. Miedaner, J. M. Dressel, D. A. Dickie, H. S. Shafaat, C. W. Machan, *J. Am. Chem. Soc.* **2021**, *143*, 13065-13073.

[11] a) C. Xiao, L. Cheng, Y. Zhu, G. Wang, L. Chen, Y. Wang, R. Chen, Y. Li, C. Li, *Angew. Chem. Int. Ed.* **2022**, *61*, e202206544; b) P. Cao, X. Quan, X. Nie, K. Zhao, Y. Liu, S. Chen, H. Yu, J. G. Chen, *Nat. Commun.* **2023**, *14*, 172.

[12] B.-H. Lee, H. Shin, A. S. Rasouli, H. Choubisa, P. Ou, R. Dorakhan, I. Grigioni, G. Lee, E. Shirzadi, R. K. Miao, J. Wicks, S. Park, H. S. Lee, J. Zhang, Y. Chen, Z. Chen, D. Sinton, T. Hyeon, Y.-E. Sung, E. H. Sargent, *Nat. Catal.* **2023**, *6*, 234-243.

[13] S. Stankovich, R. D. Piner, S. T. Nguyen, R. S. Ruoff, *Carbon* **2006**, *44*, 3342-3347.

[14] a) Z. Li, R. Ma, Q. Ju, Q. Liu, L. Liu, Y. Zhu, M. Yang, J. Wang, *Innovation (Camb)* **2022**, *3*, 100268; b) Q. Zhang, X. Tan, N. M. Bedford, Z. Han, L. Thomsen, S. Smith, R. Amal, X. Lu, *Nat. Commun.* **2020**, *11*, 4181.

[15] Z. Wei, D. WANG, S. KIM, S.-Y. KIM, Y. HU, M. K. YAKES, A. R. LARACUENTE, Z. DAI, S. R. MARDER, C. BERGER, W. P. KING, W. A. D. HEER, P. E. SHEEHAN, E. RIEDO, *Science* **2010**, *328*, 1373-1376.

[16] K. Chen, K. Liu, P. An, H. Li, Y. Lin, J. Hu, C. Jia, J. Fu, H. Li, H. Liu, Z. Lin, W. Li, J. Li, Y.-R. Lu, T.-S. Chan, N. Zhang, M. Liu, *Nat. Commun.* **2020**, *11*, 4173.

[17] Y. Li, H. Wang, Y. Li, H. Ye, Y. Zhang, R. Yin, H. Jia, B. Hou, C. Wang, H. Ding, X. Bai, A. Lu, *Nat. Commun.* **2023**, *14*, 1815.

[18] W. Li, C. Liu, C. Gu, J.-H. Choi, S. Wang, J. Jiang, *J. Am. Chem. Soc.* **2023**, *145*, 4774-4783.

[19] Y. Wang, T. Zhou, S. Ruan, H. Feng, W. Bi, J. Hu, T. Chen, H. Liu, B. Yuan, N. Zhang, W. Wang, L. Zhang, W. Chu, C. Wu, Y. Xie, *Nano Lett.* **2022**, *22*, 6622-6630.

[20] a) X. Chang, S. Vijay, Y. Zhao, N. J. Oliveira, K. Chan, B. Xu, *Nat. Commun.* **2022**, *13*, 2656; b) Y. H. Wang, S. Zheng, W. M. Yang, R. Y. Zhou, Q. F. He, P. Radjenovic, J. C. Dong, S. Li, J. Zheng, Z. L. Yang, G. Attard, F. Pan, Z. Q. Tian, J. F. Li, *Nature* **2021**, *600*, 81-85.

[21] a) B. Yang, X. Li, Q. Cheng, Q. Jia, Y. Liu, Z. Xiang, *Nano Energy* **2022**, *101*, 107565; b) Z. Pavlovic, C. Ranjan, Q. Gao, M. van Gastel, R. Schlögl, *ACS Catal.* **2016**, *6*, 8098-8105.

[22] a) S. Yang, Q. Cheng, J. Mao, Q. Xu, Y. Zhang, Y. Guo, T. Tan, W. Luo, H. Yang, Z. Jiang, *Appl. Catal. B-Environ.* **2021**, *298*, 120605; b) H. Gong, Z. Wei, Z. Gong, J. Liu, G. Ye, M. Yan, J. Dong, C. Allen, J. Liu, K. Huang, R. Liu, G. He, S. Zhao, H. Fei, *Adv. Funct. Mater.* **2021**, *32*, 2106886.

[23] J. Wei, D. Xia, Y. Wei, X. Zhu, J. Li, L. Gan, *ACS Catal.* **2022**, *12*, 7811-7820.

[24] Y. Pan, R. Lin, Y. Chen, S. Liu, W. Zhu, X. Cao, W. Chen, K. Wu, W. C. Cheong, Y. Wang, L. Zheng, J. Luo, Y. Lin, Y. Liu, C. Liu, J. Li, Q. Lu, X. Chen, D. Wang, Q. Peng, C. Chen, Y. Li, *J. Am. Chem. Soc.* **2018**, *140*, 4218-4221.

[25] a) Y. Jia, Z. Xue, J. Yang, Q. Liu, J. Xian, Y. Zhong, Y. Sun, X. Zhang, Q. Liu, D. Yao, G. Li, *Angew. Chem. Int. Ed.* **2022**, *61*, e202110838; b) A. V. Kuzmin, B. A. Shainyan, *ACS Omega* **2021**, *6*, 374-387.

[26] a) B. Hammer, J. K. Nørskov, *Nature* **1995**, *376*, 238-240; b) X. Tian, X. Zhao, Y.-Q. Su, L. Wang, H. Wang, D. Dang, B. Chi, H. Liu, E. J. M. Hensen, X. W. D. Lou, B. Y. Xia, *Science* **2019**, *366*, 850-856.

[27] S. Siahrostami, A. Verdaguer-Casadevall, M. Karamad, D. Deiana, P. Malacrida, B. Wickman, M. Escudero-Escribano, E. A. Paoli, R. Frydendal, T. W. Hansen, I. Chorkendorff, I. E. Stephens, J. Rossmeisl, *Nat. Mater.* **2013**, *12*, 1137-1143.

[28] a) Y. Hu, C. Hu, A. Du, T. Xiao, L. Yu, C. Yang, W. Xie, *Anal. Chem.* **2023**, *95*, 1703-1709; b) C. Hu, Y. Hu, C. Fan, L. Yang, Y. Zhang, H. Li, W. Xie, *Angew. Chem. Int. Ed.* **2021**, *60*, 19774-19778.

WILEY. VCH

RESEARCH ARTICLE

Table of Contents
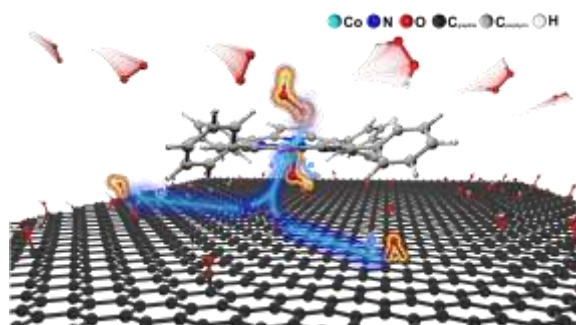
A local-environmental regulation infinitely clarifies distinguising interaction manners (remote or vicinal interaction) between different oxygen functional groups and Co center, and hence enhances the acidic H_2O_2 electrosynthesis on cobalt-porphyrin molecular catalyst.